# Supplementary Information: A single-photon emitter coupled to a phononic-crystal resonator in the resolved-sideband regime

Clemens Spinnler,[1,*] Giang N. Nguyen,[1] Ying Wang,[2] Liang Zhai,[1,4] Alisa Javadi,[1,5] Marcel Erbe,[1] Sven Scholz,[3] Andreas D. Wieck,[3] Arne Ludwig,[3] Peter Lodahl,[2] Leonardo Midolo,[2] and Richard J. Warburton[1]

[1] *Department of Physics, University of Basel, Klingelbergstrasse 82, CH-4056 Basel, Switzerland*
[2] *Center for Hybrid Quantum Networks (Hy-Q), The Niels Bohr Institute, University of Copenhagen, DK-2100 Copenhagen Ø, Denmark*
[3] *Lehrstuhl für Angewandte Festkörperphysik, Ruhr-Universität Bochum, DE-44780 Bochum, Germany*

(Dated: October 24, 2024)

## SUPPLEMENTARY NOTE 1: FINITE-ELEMENT SIMULATIONS

The mechanical resonator is simulated using Comsol Multiphysics. We perform eigenmode studies for a predefined mesh, which is optimised via a convergence test. Either fixed or lossy boundary conditions are applied to the edges of the beam. The phononic shield and the mechanical resonator are optimised to support a single mechanical in-plane breathing mode within the phononic bandgap. Figure 1(a) shows the top view of the phononic shield's unit cell. The dimensions of the etched air-hole are: $a = 970\,\text{nm}$ (lattice constant), $w = 960\,\text{nm}$ (beam width), $h = 180\,\text{nm}$ (beam thickness), $l_\text{e} = 775\,\text{nm}$ (air-hole length), and $w_\text{e} = 270\,\text{nm}$ (air-hole width). For quantum-dot (QD) charge control, we need to ensure that the gate layers show good conductance from the substrate through the phononic shield to the resonator. Therefore we try to keep the thinnest connection, between the resonator and substrate, as wide as possible, which is $(w - l_\text{e})/2 = 92.5\,\text{nm}$. For the current design, we observe about 100 MHz of additional linewidth broadening, for more information see Ref. [1].

The phononic band diagram of the unit-cell is studied by applying floquet boundary conditions in the $x$-direction. Eigenmode studies are performed upon sweeping $k_\text{x}$ from 0 to $\pi/a$, where $a$ is the lattice constant. For even and odd modes we apply symmetric and asymmetric conditions at $z = 0$, respectively. The band diagram is shown in Fig. 1(b) in the main text. We observe a complete bandgap of 0.11 GHz. We repeat the study and change the air-hole parameters by ±20 nm. Although this leads to a broadening of the bands, the width of the phononic gap is not much affected (especially for even modes). This suggests that the phononic shield is relatively robust against small deviations from the original design. From the band diagram study, we can also extract the density of states (DOS), shown in Fig. 1(b). We sum the obtained eigenmodes over a specific frequency bandwidth and normalise the states to the unit-cell length [2]:

$$\text{DOS} = \frac{n_{\Delta f}}{\Delta f \cdot n_\text{k} \cdot a}, \tag{1}$$

where $\Delta f$ is the frequency bandwidth, $n_{\Delta f}$ is the number of modes in $\Delta f$, $n_\text{k}$ is the number of $k$-points in our study, and $a$ is the unit-cell length.

To estimate how many phononic-shield elements are needed, such that the resonator's damping is not limited by clamping losses, we perform a mechanical-quality-factor study in dependence on the number of shield unit cells, see Fig. 1(c). The study is performed by applying a lossy boundary condition at the two beam ends. Since no phonon loss within the material is added, this only simulates clamping losses. We select seven air holes (yellow line) on each side of the resonator.

To finalise our design, we perform an optical far-field study of an emitter placed in the centre of the mechanical resonator and we optimise the beam width and resonator defect length ($x$-direction) for radiation to the top (collection lens). For a width of 960 nm, the two sidewalls reflect the field within the beam such that there is constructive interference, increasing the radiation of the field to the top [1].

To estimate the exciton-phonon coupling rate, we perform thermomechanical calibration [3]. We describe the system by a linear harmonic oscillator via the displacement function:

$$u(r,t) = x(t)|u(r)|, \tag{2}$$

where $|u(r)| = \frac{u(r)}{\max(|u(r)|)}$ describes the normalised mode profile [3] obtained from COMSOL, and $x(t)$ describes the time dependence of the periodic motion. The equation of motion is:

$$m_\text{eff}\frac{dx^2(t)}{dt^2} + m_\text{eff}\Gamma_\text{m}\frac{dx(t)}{dt} + m_\text{eff}\Omega_\text{m}^2 x(t) = F(t), \tag{3}$$

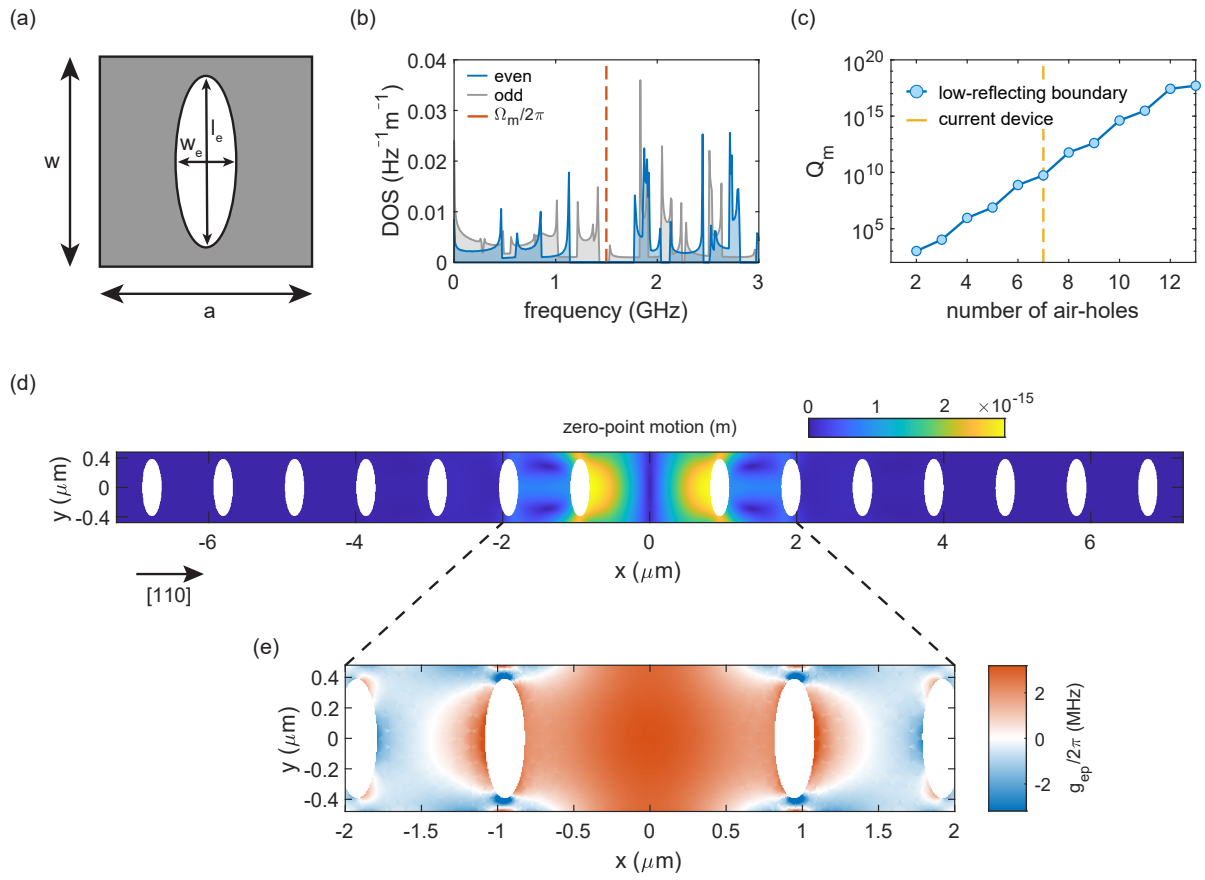


Supplementary Fig. 1. **Finite-element simulations. (a)** Top view of the phononic-shield unit cell which consists of an elliptical air-hole: a = 970 nm (lattice constant), w = 960 nm, h = 180 nm (beam thickness), $l_e$ = 775 nm, and $w_e$ = 270 nm. **(b)** Mechanical density of states (DOS) for even (in-plane/symmetric) and odd (out-of-plane/asymmetric) modes. The mechanical frequency is designed to lie in the centre of the complete bandgap. The simulation is performed with $n_k = 2000$ and $\Delta f = 8$ MHz. **(c)** Mechanical quality factor with increasing number of shield unit cells. For the device presented in the main paper, seven unit cells were chosen. **(d)** Thermal displacement of an eigenmode study obtained via thermomechanical calibration. The major displacement of the in-plane breathing mode is along the beam axis. **(e)** Exciton-phonon coupling rate based on deformation potential coupling, evaluated in the centre of the membrane (QD layer). A coupling rate of $g_{ep}/2\pi = 3.2$ MHz is found in the centre of the resonator.

where $\Omega_m/2\pi$ is the mechanical frequency, $k = m_{eff}\Omega_m^2$ is the spring constant, and $\Gamma_m$ is the energy dissipation rate which relates to the mechanical quality by $Q_m = \Omega_m/\Gamma_m$. The effective mass and zero-point-motion are obtained with:

$$m_{eff} = \int \rho \left( \frac{u(r)^2}{\max(|u(r)|)^2} \right) dV \tag{4}$$

$$x_{zpf} = \sqrt{\frac{\hbar}{2 m_{eff} \Omega_m}}, \tag{5}$$

where $\rho$ is the material density of GaAs, and $\hbar$ is the reduced Planck constant. Figure 1(d) shows the displacement, $x_{zpf} \cdot |u(r)|$, of the in-plane breathing mode. The thermal displacement (Brownian-motion) is then given by the equipartition theorem [4]:

$$x_{th} = x_{zpf} \sqrt{\frac{2 k_B T}{\hbar \Omega_m}}, \tag{6}$$

where $T$ is the phonon-bath temperature, and $k_B$ is the Boltzmann constant. The exciton-phonon coupling is extracted

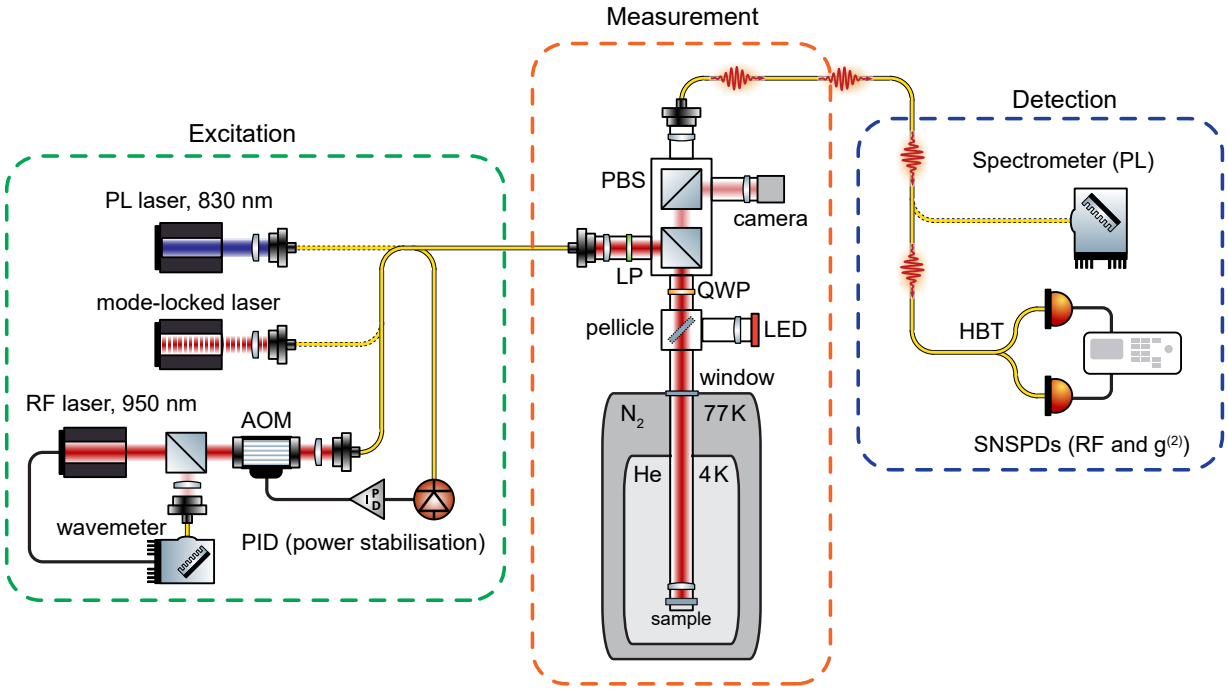


Supplementary Fig. 2. **Optical setup including all relevant hardware for excitation, measurement, and detection.** A double-pass acousto-optic modulator setup is used to stabilise the RF laser power. The excitation laser is fibre-coupled and sent to the dark-field microscope. With two PBS, an LP, and a QWP, the reflected laser light is suppressed. The collected QD single-photons are also fibre-coupled and analysed using SNSPDs. PL: photoluminescence, RF: resonance fluorescence, PBS: polarising beam splitter, LP: linear polariser, QWP: quarter-wave plate, HBT: Hanbury Brown-Twiss, SNSPDs: superconducting-nanowire single-photon detectors.

from the strain profile after normalising the displacement by the zero-point motion. The QD couples to the strain via deformation potential coupling [4, 5]:

$$\Delta E = a(\epsilon_{xx} + \epsilon_{yy} + \epsilon_{zz}) - \frac{b}{2}(\epsilon_{xx} + \epsilon_{yy} - 2\epsilon_{zz}), \tag{7}$$

where $\Delta E$ is the QD's energy shift, $a = -8.33$ $e$V and $b = -1.7$ $e$V are the deformation potentials for the hydrostatic and shear strain of GaAs, respectively [6, 7]. The exciton-phonon coupling rate $g_{\mathrm{ep}}$ is:

$$g_{\mathrm{ep}} = \frac{\partial \omega_{\mathrm{QD}}}{\partial x} x_{\mathrm{zpf}} = \frac{\Delta E}{\hbar}. \tag{8}$$

Figure 1(e) shows $g_{\mathrm{ep}}/2\pi$ for the in-plane breathing mode. In the very centre of the resonator, which is the optimal position for the QD location, we obtain $g_{\mathrm{ep}}/2\pi = 3.2\,\mathrm{MHz}$.

## SUPPLEMENTARY NOTE 2: DEVICE FABRICATION AND MEASUREMENT SETUP

The wafer material is grown with molecular-beam epitaxy and consists of a 1.15 µm AlAs sacrificial layer and a 180 nm GaAs diode structure. The diode consists of a QD-layer at the centre of the membrane (at $z = 0$), as well as the p- and n-doped layers at the top and the bottom, respectively. The advantage of the QD-in-middle device is that the dots couple strongly to mechanical in-plane breathing modes. Above the QDs, there is an $Al_{0.33}Ga_{0.67}As$ blocking layer, to minimise the diode leakage current. Details on the wafer material can be found in Ref. [1].

The mechanical resonator is fabricated by means of electron-beam lithography. First, the mesa structure is etched and $1.5\times$ $1\,\mu m^2$ contact pads are evaporated: Ni/Ge/Au/Ni/Au for the back contact (which is annealed to form an ohmic contact) and Cr/Au for the top contact. Second, using a soft mask, the nanostructures are written using an electron-beam and dry etched [8, 9] into the membrane (inductively-coupled plasma reactive ion etching). Finally,

after removing the residual resist, the structures are under-etched in a wet-etch process (hydrofluoric acid) and released via critical-point drying [9]. During the fabrication of the mechanical resonators, the design axis (x-axis in Fig. 1(d)) is aligned with the [110] axis of the wafer. Since the mechanical properties of GaAs are anisotropic, the current mechanical mode would shift to 1.25 GHz when aligning to [100].

The sample is glued onto a titanium sample holder using non-conductive two-component epoxy (UHU, endfest 300) and the contacts are connected manually to a PCB using copper wires and silver epoxy (EPO-TEK, E4110). The sample is mounted on x/y/z-piezo steppers (attocube, ANPx101 & ANPz101) and an x-y-scanner (attocube, ANSxy100lr) in a home-built vacuum-tube microscope with an optical NA = 0.65. The tube is evacuated down to $4 \times 10^{-6}$ mbar and then filled with 0.2 mbar helium exchange gas, corresponding to $2.8 \times 10^{-3}$ mbar at 4.2 K. At this gas pressure, gas damping is negligible, see Ref. [1]. The measurement tube is precooled to liquid nitrogen temperature (77 K) and then moved into the He-bath cryostat (Cryovac) at 4.2 K. The full measurement setup is shown in Fig. 2.

The gate voltage of the sample is controlled with a digital-to-analogue converter (Basel Precision Instruments, DAC SP 927). The optical excitation part of the setup consists of three different lasers: a diode laser for photoluminescence excitation at 830 nm (PicoQuant, LDH-D-C-830), a mode-locked laser for radiative-lifetime measurements (Coherent, Mira 900-D), and a tunable diode laser for resonant excitation around 950 nm (Toptica, DL pro). The resonant laser is frequency stabilised with a wavemeter (HighFinesse, WS7) and power stabilised with a double-pass acousto-optic modulator setup (Gooch and Housego, AOM 3200-1113 & AODR 1200AF-AINA-2.5 HCR). All lasers are fibre-coupled (Thorlabs, SM-780HP) and sent to the cross-polarised optical microscope. The microscope consists of two polarising beam splitters, a linear polariser, and a quarter-waveplate. A laser suppression of up to $10^{-8}$ is typically achieved when the beam is focused on bulk GaAs [10]. The sample surface can be imaged using a camera (Allied Vision, Guppy) in combination with an LED (Thorlabs, M940D2) and a removable pellicle beamsplitter (Thorlabs, BP145B2). The field of view is around 10 $\mu$m. The collected QD photons are fibre-coupled and sent to either a spectrometer (Teledyne Princeton Instruments, Blaze 100HRX & Acton SP2500i) or single-photon detectors in a Hanbury Brown-Twiss setup (Single Quantum, Eos & Swabian Instruments, Time Tagger Ultra).

## SUPPLEMENTARY NOTE 3: OPTICAL CHARACTERISATION OF THE QUANTUM DOT

For the thermal-motion measurements, it is essential to find a QD that not only has a high exciton-phonon coupling rate but also a high count rate, a low inhomogeneous broadening, and good laser suppression. We present here additional QD characterisation measurements to those shown in the main text. In the following paragraphs (also in the main text), we refer to the frequency jittering of the QD resonance as the inhomogeneous broadening. The line broadening due to excited-state dephasing, we refer to as the homogeneous broadening of the QD, also see Ref. [11].

To estimate the inhomogeneous broadening, we compare the measured linewidth to the transform limit, see Fig. 2(d) in the main text. To determine the lifetime, we excite the QD using picosecond optical pulses. The time tagger module is synchronised with the pulsed laser and a time histogram is recorded, see Fig. 3(a). The excited state of the QD ($X^{1-}$) freely decays with a time constant of $\tau_\mathrm{R} = 1.18$ ns. This gives an excited-state decay rate of $\Gamma_\mathrm{R} = 1/\tau_\mathrm{R} = 847$ MHz, with a corresponding transform-limited linewidth of $\Gamma_\mathrm{R}/2\pi = 135$ MHz. A low-power linewidth measurement is presented in the main text, which yields $\Gamma_\mathrm{inh}/2\pi = 550$ MHz, which is a factor of four above the transform limit.

The Rabi frequency, $\Omega_\mathrm{R}$, describes the interaction strength of the laser with the QD. We convert the excitation power to the Rabi frequency by carrying out a resonant power-saturation measurement, see Fig. 3(b). Each data point represents the peak intensity of a linewidth scan (obtained from a Lorentzian fit) at the corresponding excitation power. The QD count rate is proportional to the excited-state population, $\rho_\mathrm{ee}$, which is given by [1]:

$$\langle \hat{\sigma}_+ \hat{\sigma}_- \rangle = \rho_{ee} = \frac{\left(\frac{1}{2}\Omega_\mathrm{R}\right)^2}{\Delta\omega_\mathrm{l}^2 + \frac{1}{2}\Omega_\mathrm{R}^2 + \left(\frac{1}{2}\Gamma_\mathrm{R}\right)^2}, \tag{9}$$

where $\Omega_\mathrm{R}$ is the Rabi frequency, $\Delta\omega_\mathrm{l}/2\pi$ is the laser detuning from the QD transition, and $\Gamma_\mathrm{R}$ is the excited-state decay rate. By fitting Eq. 9 to the data, the excitation power is translated to $\Omega_\mathrm{R}$. Here, we include the inhomogeneous broadening by a convolution of Eq. 9 with a Lorentzian-weighted detuning jitter of 400 MHz. Without this, the Rabi frequency would be underestimated, yellow line in Fig. 3(b).

The ratio between unsuppressed laser and QD counts depends highly on the laser spot position which in turn depends on the QD position. Furthermore, it also highly depends on the excitation power. Figure 3(c) shows a low-power autocorrelation measurement, with 5 nW of laser power reaching the sample ($\Omega_\mathrm{R} \ll \Gamma_\mathrm{R}$). The high single-photon purity of 98 % proves that the QD acts as a single-photon emitter. The autocorrelation is fitted with the standard autocorrelation function of a two-level system [12].

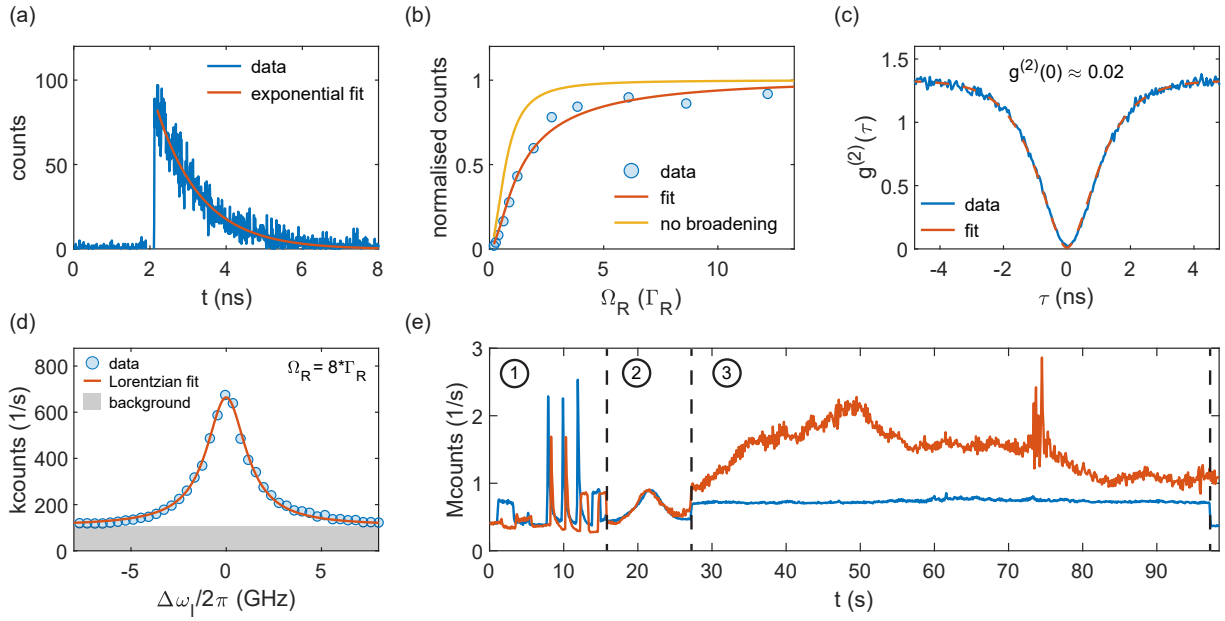


Supplementary Fig. 3. **Optical characterisation of the QD. (a)** Radiative-lifetime measurement with $\tau = 1.18\,\mathrm{ns}$. The corresponding transform limit for the linewidth is $1/(2\pi\tau_R) = 135\,\mathrm{MHz}$. **(b)** Resonant saturation-power curve. The excitation power is converted to the Rabi frequency, $\Omega_R$, via a model fit to the data (orange curve). **(c)** Low-power ($\Omega_R \ll \Gamma_R$) autocorrelation measurement. Due to the high level of laser suppression, a single-photon purity of 98 % is achieved. **(d)** High-power resonant linewidth scan with $\Omega_R = 8\ \Gamma_R$. **(e)** Two example time traces (blue and red) of a high-power autocorrelation measurement: (1) automatic laser suppression, (2) locking of the QD resonance, and (3) autocorrelation measurement.

At high excitation powers ($\Omega_R \gg \Gamma_R$) the emission of the quantum emitter saturates, however, the unsuppressed laser increases. This leads to a reduced signal-to-background level. Figure 3(d) shows a high-power linewidth scan, where the background level is significant (compared to Fig. 2(d) in the main text). The signal-to-background increases further upon detuning the laser from resonance. Therefore, in an autocorrelation measurement, the higher the laser power and the higher the laser detuning, the lower the single-photon purity (higher $g^{(2)}(0)$). In addition, the background level is also very unstable. Figure 3(e) shows two example time traces of a high-power ($\Omega_R = 8\ \Gamma_R$) autocorrelation measurement with a laser detuning of $\Delta\omega_l/2\pi = 1\,\mathrm{GHz}$. The measurement is performed as follows. First, the laser is automatically suppressed by alternately optimising the linear polariser and quarter-wave-plate angles in our dark-field microscope. Second, we perform a linewidth scan and lock the QD resonance to the laser frequency, thus, compensating for spectral drifts. Third, autocorrelation data is recorded for one minute, followed by going back to step one. During the measurement, the laser suppression can drift up to an order of magnitude, a result of a slight change in laser spot position due to vibrational noise from the environment and pressure changes in the helium recovery line.

## SUPPLEMENTARY NOTE 4: FROM AUTOCORRELATION TO NOISE-POWER SPECTRUM

In our experiments, we acquire the noise-power spectrum via an autocorrelation measurement. As mentioned above, the collected signal contains unsuppressed laser light, which does not carry information about the mechanical resonator. Therefore, to obtain the true mechanical noise power, we need to correct for the unsuppressed laser. The unsuppressed laser results in a flat background in the autocorrelation measurement (see Fig. 4(a), black curve), which we correspondingly subtract. Subsequently, the autocorrelation is normalised to one at large time delays (ms-regime). Figure 4(a) shows the post-processed autocorrelation, performed at optimal detuning such that $\Omega_R^{\mathrm{eff}} = \Omega_m$. At long time delays, weak oscillations due to the interaction with the mechanical resonator are visible (also see main paper). The prominent oscillations at short delays are Rabi oscillations at $\Omega_R^{\mathrm{eff}}$. The noise-power spectrum is related to the autocorrelation via a Fourier transform (Wiener–Khinchin theorem) [5]:

$$S_{\mathrm{nn}}(f) = 2\mathrm{FFT}\left[g^{(2)}(\tau)\right]\tau_{\mathrm{bin}}, \tag{10}$$

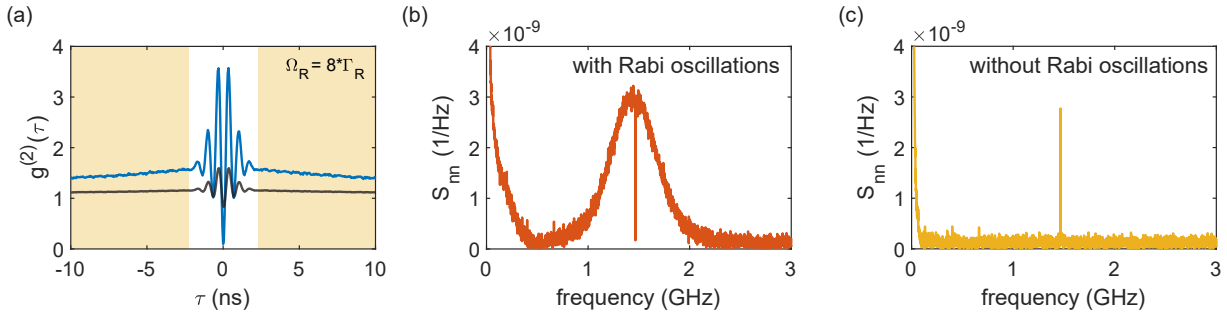


Supplementary Fig. 4. **From autocorrelation to noise-power spectrum. (a)** Autocorrelation measurement at optimal detuning, $\Omega_R^{\text{eff}} = \Omega_m$, before (black) and after (blue) correcting for the unsuppressed laser. This is the same measurement as in the main text in Fig. 3(h). **(b)** Fourier transform of the full autocorrelation data which is shown in (a). **(c)** Fourier transform of the autocorrelation data without Rabi oscillations, yellow shaded area in (a).

where $g^{(2)}(\tau)$ is the normalised autocorrelation data, and $\tau_{\text{bin}}$ is the autocorrelation binning time. Figure 4(b) shows $S_{\text{nn}}(f)$ obtained from the full autocorrelation data. The broad peak around 1.5 GHz is associated with the strong but rapidly decaying Rabi oscillations from Fig. 4(a). The sharp feature is due to the QD-mechanical interaction. Due to a phase difference of $\pi$ between Rabi oscillations and mechanical modulation, the mechanical noise peak appears as a dip in the broad Rabi peak. This makes it hard to integrate the mechanical-noise peak. To remove the Rabi oscillations, we perform the Fourier transform on the data at delays $\tau > \tau_R$ (yellow region in Fig. 4(a)), once the Rabi oscillations are completely damped. The corresponding noise-power spectrum shows the mechanical noise as a peak on a flat background, see Figure 4(c). This process does not compromise the mechanical noise power since the mechanical damping constant of $\tau_m = 2Q_m/\Omega_m = 0.46\,\mu$s is several orders of magnitudes larger than the Rabi damping of $\approx 1$ ns.

## SUPPLEMENTARY NOTE 5: MASTER-EQUATION SIMULATIONS

To simulate the exciton-phonon interaction we perform master-equation simulations. The full Hamiltonian of the system is given by:

$$\hat{H} = \hat{H}_{\text{QD}} + \hat{H}_{\text{m}} + \hat{H}_{\text{int}} + \hat{H}_{\text{drive}}, \tag{11}$$

where $\hat{H}_{\text{QD}}$ is the QD, $\hat{H}_{\text{m}}$ the mechanical, $\hat{H}_{\text{int}}$ the interaction, and $\hat{H}_{\text{drive}}$ the optical drive part. We describe the QD as a simple two-level system (TLS) with a ground and an excited state, $|g\rangle$ and $|e\rangle$, respectively. The TLS is driven by a classical optical field. In the dipole approximation, this reads:

$$\hat{H}_{\text{QD}} + \hat{H}_{\text{drive}} = \hbar\omega_{\text{QD}}\hat{\sigma}_+\hat{\sigma}_- - \hbar\frac{\Omega_R}{2}\left(\hat{\sigma}_+ + \hat{\sigma}_-\right)\left(e^{i\omega_l t} + e^{-i\omega_l t}\right), \tag{12}$$

where $\hbar\omega_{\text{QD}}$ is the QD's exciton transition energy, $\Omega_R$ is the optical Rabi frequency, $\omega_l/2\pi$ is the frequency of the driving field, $\hat{\sigma}_+ = |e\rangle\langle g|$ and $\hat{\sigma}_- = |g\rangle\langle e|$ are the Pauli transition operators. The mechanical part is described by a quantum harmonic oscillator:

$$\hat{H}_{\text{m}} = \hbar\Omega_m\left(\hat{b}^\dagger\hat{b} + 1/2\right), \tag{13}$$

where $\Omega_m/2\pi$ is the mechanical frequency, $\hat{b}^\dagger$ and $\hat{b}$ are the phonon creation and annihilation operators, respectively. The phonon occupation of the mechanical resonator is $\langle n_m\rangle = \langle\hat{b}^\dagger\hat{b}\rangle$. The interaction part between the two systems has a dispersive form where the displacement leads to a shift in the excited-state energy of the QD:

$$\hat{H}_{\text{int}} = \hbar g_{\text{ep}}\hat{\sigma}_+\hat{\sigma}_-\left(\hat{b}^\dagger + \hat{b}\right), \tag{14}$$

where $g_{\text{ep}}/2\pi$ is the exciton-phonon coupling rate, $\hat{\sigma}_+\hat{\sigma}_- = |e\rangle\langle e|$, and $(\hat{b}^\dagger + \hat{b}) = \hat{x}/x_{\text{zpf}}$ is the displacement operator in units of the zero-point motion. The interaction part can also be described classically:

$$\hat{H}_{\text{int}} = \hbar\frac{g_{\text{ep}}}{x_{\text{zpf}}}x_{\text{th}}\sin(\Omega_m t)\hat{\sigma}_+\hat{\sigma}_- = \hbar g_{\text{ep}}^{\text{th}}\sin(\Omega_m t)\hat{\sigma}_+\hat{\sigma}_-, \tag{15}$$

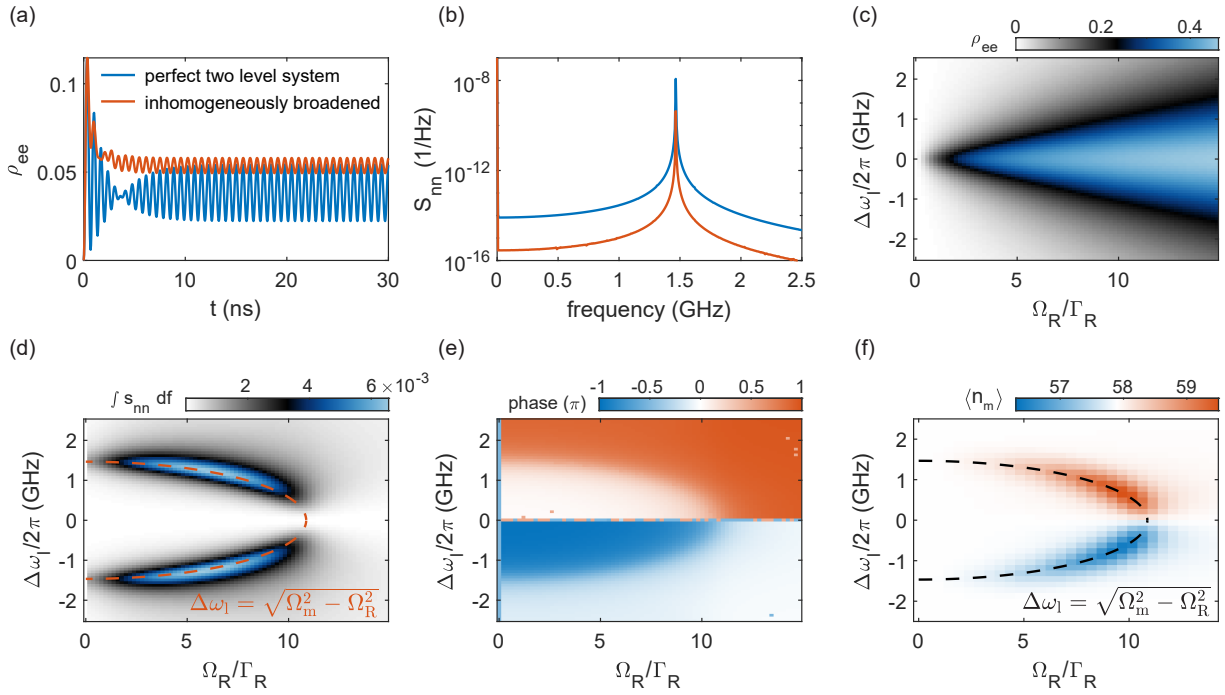


Supplementary Fig. 5. **Master equation simulations** with a classical (a-e) and a quantum description (f) of the mechanical resonator. **(a)** Numerical simulation of the excited-state population, showing a modulation due to the mechanical vibrations. **(b)** Fourier transform of the data shown in (a). **(c)** Steady-state (time-averaged) excited-state population in dependence of the laser detuning and Rabi frequency. **(d)** Integrated mechanical-noise peak, and **(e)** phase of the modulation. **(f)** Expectation value of the phonon occupation upon detuning the laser blue (heating) or red (cooling). The simulation parameters are: $\tau_R = 1.18\,\mathrm{ns}$, $\Omega_m/2\pi = 1.466\,\mathrm{GHz}$, $g_{ep}^{th}/2\pi = 34.4\,\mathrm{MHz}$, $g_{ep}/2\pi = 3.2\,\mathrm{MHz}$, and $\langle n_m \rangle = 58$.

where $x_{th}$ is the thermal displacement, and $g_{ep}^{th} = g_{ep}\sqrt{2\langle n_m \rangle} = 2\pi\times 34.4\,\mathrm{MHz}$ is the thermal exciton-phonon coupling rate [13]. In the rotating frame of the laser field, the full Hamiltonian reads:

$$\hat{H}_{RWA} = -\hbar\Delta\omega_l\hat{\sigma}_+\hat{\sigma}_- + \hbar\Omega_m\left(\hat{b}^\dagger\hat{b} + 1/2\right) + \hbar g_{ep}\hat{\sigma}_+\hat{\sigma}_-\left(\hat{b}^\dagger + \hat{b}\right) + \hbar\frac{\Omega_R}{2}\left(\hat{\sigma}_+ + \hat{\sigma}_-\right), \tag{16}$$

where $\hbar\Delta\omega_l$ is the energy detuning between the driving field and the QD transition. The incoherent part of the Hamiltonian, which is the QD's radiative decay, is added via a Lindblad operator $\hat{L} = \sqrt{\Gamma_R}\hat{\sigma}_-$. The time dynamic of the system is captured by the von Neumann equation [14]:

$$\frac{\partial}{\partial t}\hat{\rho} = -\frac{i}{\hbar}[\hat{H}_{RWA}, \hat{\rho}] + \hat{\mathcal{L}}(\hat{\rho}), \quad \hat{\mathcal{L}}(\hat{\rho}) = \frac{1}{2}\left(2\hat{L}\hat{\rho}\hat{L}^\dagger - \hat{\rho}\hat{L}^\dagger\hat{L} - \hat{L}^\dagger\hat{L}\hat{\rho}\right). \tag{17}$$

In our first simulation, we reproduce the time-modulation in the QD's emission upon detuning the probe laser field. Since the phonon population is large, $\langle n_m \rangle = 58 \gg 1$, the interaction can be expressed classically [15], excluding backaction on the mechanical resonator. Furthermore, we assume that the phase of the mechanical resonator is static on the time scales of the QD dynamics (few ns). We perform numerical simulations using Eq.16-17 and solve for the excited-state population, $\rho_{ee}$. The inhomogeneous broadening is included by a Lorentzian-weighted detuning jitter of 400 MHz. Figure 5(a) shows $\rho_{ee}$ as a function of time without (blue) and with (orange) inhomogeneous broadening, respectively. Laser detuning and Rabi frequency are chosen such that $\Omega_R^{eff} = \Omega_m$. The strong oscillations at short $t$ are the optical Rabi oscillations and the weaker oscillations arise due to the QD-mechanical coupling. Note that, in general, the mechanical modulation shows a higher amplitude in the time trace than in the autocorrelation. Around 3 ns, the phase shifts from the Rabi to the mechanical oscillations. The simulation is performed over 300 mechanical periods, where we analyse further only the final 50 periods. As for the autocorrelation, we obtain the noise-power spectrum via a Fourier transform of the normalised time trace:

$$S_{nn}(f) = 2\mathrm{FFT}\left[\frac{\rho_{ee}(t)}{\langle\rho_{ee}\rangle}\right]^2\frac{t_{bin}^2}{t_{sim}}, \tag{18}$$

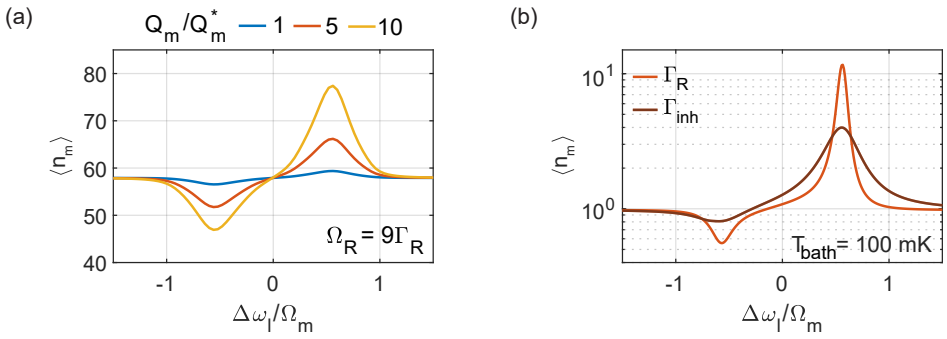


Supplementary Fig. 6. **Mechanical backaction at optimal driving parameters. (a)** Expectation value of the phonon population of the mechanical resonator with increasing mechanical quality factor at 4.2 K. $Q_{\mathrm{m}}^{*}$ corresponds to the current device parameter of $2.1 \times 10^3$. **(b)** Phonon occupation of the resonator with $Q_{\mathrm{m}} = 10^4$ and $g_{\mathrm{ep}}/2\pi = 2 \times 3.2$ MHz on starting at millikelvin temperatures, with (dark line) and without (bright line) inhomogeneous broadening.

where $\langle \rho_{\mathrm{ee}} \rangle$ is the average excited-state population, $t_{\mathrm{bin}}$ is the binning time, and $t_{\mathrm{sim}}$ is the length of the simulation. Figure 5(b) shows $S_{\mathrm{nn}}(f)$ obtained from the simulation shown in Fig. 5(a). Comparing the simulations without and with inhomogeneous broadening, we observe an order-of-magnitude reduction in signal strength.

The numerical simulations are performed upon sweeping the Rabi frequency and laser detuning. Figure 5(c) shows the time-averaged excited-state population. The integrated noise-power of the mechanical modulation is shown in Fig. 5(d). As can be seen, the highest interaction between the two systems is found when the effective Rabi frequency matches the mechanical frequency:

$$\Omega_{\mathrm{R}}^{\mathrm{eff}} = \sqrt{\Omega_{\mathrm{m}}^2 + \Delta\omega_{\mathrm{l}}^2} \stackrel{!}{=} \Omega_{\mathrm{m}}. \tag{19}$$

At low excitation powers ($\Omega_{\mathrm{R}} \ll \Omega_{\mathrm{m}}$), this corresponds to detuning the laser to one of the acoustic sidebands $\Delta\omega_{\mathrm{l}} = \pm\Omega_{\mathrm{m}}$. Conversely, at high excitation powers ($\Omega_{\mathrm{R}} > \Omega_{\mathrm{m}}$), this corresponds to $\Delta\omega_{\mathrm{l}} = \sqrt{\Omega_{\mathrm{m}}^2 - \Omega_{\mathrm{R}}^2}$ (highlighted in orange). Figure 5(e) shows the phase of the excited state's time modulation. Several transitions of $\pi$ are visible, matching with the resonance condition of $\Omega_{\mathrm{R}}^{\mathrm{eff}} = \Omega_{\mathrm{m}}$. Note that the signal-to-noise ratio in the measured power spectrum depends on the product of Fig. 5(c) and (d), which is the noise sensitivity multiplied by the excited-state population (photon count rate).

In order to extract the degree of mechanical cooling, we perform a second simulation where we include the backaction on the phonon population of the mechanical resonator. For this, the mechanical resonator is treated as a quantum harmonic oscillator coupled to a thermal bath. To reduce simulation time, we make use of the quantum simulation toolbox Qutip [16, 17]. We perform master-equation simulations using Eq. 16 and 17, solving for the steady-state solution. The coupling to the thermal bath is described with additional collapse operators:

$$\hat{c}_{\mathrm{in}} = \sqrt{\Gamma_{\mathrm{m}} \cdot n_{\mathrm{bath}}} \cdot \hat{b}^{\dagger}, \qquad \hat{c}_{\mathrm{out}} = \sqrt{\Gamma_{\mathrm{m}} \cdot (n_{\mathrm{bath}} + 1)} \cdot \hat{b}, \tag{20}$$

where $\Gamma_{\mathrm{m}} = \Omega_{\mathrm{m}}/Q_{\mathrm{m}}$ is the energy dissipation rate, and $n_{\mathrm{bath}} = 58$ is the thermal-bath population (at $\Omega_{\mathrm{m}}$, $T = 4.2$ K). The simulations are performed with an $N_{\mathrm{m}} = 500$ dimensional mechanical Hilbert space. Also here, 400 MHz of inhomogeneous broadening is included.

Figure 5(f) shows the expectation value of the resonator's phonon population, $\langle n_{\mathrm{m}} \rangle$, as a function of Rabi frequency and laser detuning. As before, the strongest interaction is found when $\Omega_{\mathrm{R}}^{\mathrm{eff}} = \Omega_{\mathrm{m}}$. To observe a change in phonon population, high excitation powers and laser detunings smaller than $\Omega_{\mathrm{m}}$ are required. Figure 6(a) shows $\langle n_{\mathrm{m}} \rangle$ at optimal laser power and laser detuning for quality factors of 1, 5, and 10 times the current value. With the current device properties (blue curve), the change in phonon number is small. However, when increasing the mechanical quality factor, substantial cooling can be observed (orange and yellow curves). Figure 6(b) shows $\langle n_{\mathrm{m}} \rangle$ for a five-fold enhanced $Q_{\mathrm{m}}$, a two-fold increased $g_{\mathrm{ep}}$, and a transform-limited linewidth (bright red curve). Even though the current quantum dot has a narrow optical linewidth with $\Gamma_{\mathrm{inh}} = 4\Gamma_{\mathrm{R}}$, the remaining inhomogeneous broadening reduces the change in phonon population by more than a factor of two (dark red curve).

* c.spinnler@unibas.ch
[4] Current address: Institute of Fundamental and Frontier Sciences, University of Electronic Science and Technology of China, Chengdu, 610054, P. R. China
[5] Current address: School of Electrical and Computer Engineering, University of Oklahoma, Norman, OK 73019, USA

[1] Spinnler, C. Exploiting phonon and Coulomb interactions in semiconductor quantum dots. *PhD Thesis, University of Basel* (2023).
[2] Florez, O. *et al.* Engineering nanoscale hypersonic phonon transport. *Nat. Nanotechnol.* **17**, 947–951 (2022).
[3] Hauer, B. D., Doolin, C., Beach, K. S. D. & Davis, J. P. A general procedure for thermomechanical calibration of nano/micro-mechanical resonators. *Ann. Phys.* **339**, 181–207 (2013).
[4] Yeo, I. *et al.* Strain-mediated coupling in a quantum dot–mechanical oscillator hybrid system. *Nat. Nanotechnol.* **9**, 106–110 (2014).
[5] Munsch, M. *et al.* Resonant driving of a single photon emitter embedded in a mechanical oscillator. *Nat. Commun.* **8**, 76 (2017).
[6] Vurgaftman, I., Meyer, J. R. & Ram-Mohan, L. R. Band parameters for III–V compound semiconductors and their alloys. *J. Appl. Phys.* **89**, 5815–5875 (2001).
[7] Van de Walle, C. G. Band lineups and deformation potentials in the model-solid theory. *Phys. Rev. B* **39**, 1871–1883 (1989).
[8] Midolo, L., Pregnolato, T., Kiršanskè, G. & Stobbe, S. Soft-mask fabrication of gallium arsenide nanomembranes for integrated quantum photonics. *Nanotechnology* **26** (2015).
[9] Uppu, R. *et al.* Scalable integrated single-photon source. *Sci. Adv.* **6**, eabc8268 (2020).
[10] Kuhlmann, A. V. *et al.* A dark-field microscope for background-free detection of resonance fluorescence from single semiconductor quantum dots operating in a set-and-forget mode. *Rev. Sci. Instrum.* **84**, 073905 (2013).
[11] Zhai, L. *et al.* Quantum interference of identical photons from remote GaAs quantum dots. *Nat. Nanotechnol.* **17**, 829–833 (2022).
[12] Jahn, J.-P. *et al.* An artificial Rb atom in a semiconductor with lifetime-limited linewidth. *Phys. Rev. B* **92**, 245439 (2015).
[13] Leijssen, R., La Gala, G. R., Freisem, L., Muhonen, J. T. & Verhagen, E. Nonlinear cavity optomechanics with nanomechanical thermal fluctuations. *Nat. Commun.* **8**, ncomms16024 (2017).
[14] Gerry, C. & Knight, P. *Cambridge University Press* (2004).
[15] Weiß, M. *et al.* Optomechanical wave mixing by a single quantum dot. *Optica* **8**, 291–300 (2021).
[16] Johansson, J. R., Nation, P. D. & Nori, F. QuTiP: An open-source Python framework for the dynamics of open quantum systems. *Comput. Phys. Commun.* **183**, 1760–1772 (2012).
[17] Johansson, J. R., Nation, P. D. & Nori, F. Qutip 2: A python framework for the dynamics of open quantum systems. *Comput. Phys. Commun.* **184**, 1234–1240 (2013).